ELSEVIER

Journal of Nuclear Materials 266–269 (1999) 928–933

journal of nuclear materials

Drift effects in W7-AS limiter and island divertor configurations

Y. Feng *, F. Sardei [1], P. Grigull, G. Herre, W7-AS Team

Max-Planck-Institut für Plasmaphysik, EURATOM Ass., D-85748 Garching, Germany

Abstract

Typical B-direction dependent asymmetries observed in the limiter and island SOL of W7-AS low-density ECRH discharges are shortly reviewed and explained in terms of classical drifts. While grad-B drifts are responsible for the up/down asymmetries of the limiter load, $\boldsymbol{E}\times\boldsymbol{B}$ drifts associated with temperature inhomogeneities in the plasma give rise to asymmetric plasma distributions in the limiter and island SOL. After a careful analysis of the transport implications of these drifts, simple 1D and 2D models have been defined, which reproduce consistently the experimental observations. The main results are confirmed by more rigorous treatment based on the 3D Monte Carlo transport code EMC3.

Keywords: W7-AS; Drifts; Island divertor

1. Introduction

For low density, low recycling ECRH discharges in W7-AS, B-direction dependent asymmetries of the plasma distribution in the SOL and of the power deposition and particle fluxes on the target plates have been observed for both limiter ($\iota < 0.4$) and island divertor ($\iota \geqslant 0.5$) configurations [1–3]. In both cases the asymmetries can be explained by classical drift effects.

In tokamaks, classical drifts have been shown to also affect the asymmetries of power and particle fluxes between the inner and outer divertor branches [4]. In particular, the $\boldsymbol{E}\times\boldsymbol{B}$ drift contributions to the cross-field particle transport can be of the same order of magnitude as that of the anomalous particle transport and of the poloidal component of the parallel transport, as estimated by Chankin for a typical tokamak scrape-off layer (SOL) [5]. Therefore, these terms have been included recently in several 2D edge transport codes in addition to the usual anomalous terms [6–8].

Classical particle drifts can be expressed either in guiding centre or fluid approximation [5,9]. In the fluid approximation, which is commonly used in the edge transport codes, the classical cross-field particle flux density, which includes all relevant drifts, can be written in the form [8]

$$n\boldsymbol{V}_\perp = \frac{n}{B^2}\boldsymbol{E}\times\boldsymbol{B} + \nabla\times\left(-\frac{p_{\mathrm{i}\perp}\boldsymbol{B}}{\mathrm{e}B^2}\right) + \frac{p_{\mathrm{i}\perp}\boldsymbol{B}}{\mathrm{e}B^3}\boldsymbol{B}\cdot\nabla\times\frac{\boldsymbol{B}}{B} + \frac{p_{\mathrm{i}\perp}}{\mathrm{e}B^3}\boldsymbol{B}\times\nabla B + \frac{P_{\mathrm{i}\parallel} + mnV_\parallel^2}{\mathrm{e}B^3}\boldsymbol{B}\times\left(\boldsymbol{B}\cdot\nabla\frac{\boldsymbol{B}}{B}\right) \tag{1}$$

to first order in r_λ/L, with r_λ the Larmor radius and L the relevant gradient scale length. The first term on the right-hand side is the $\boldsymbol{E}\times\boldsymbol{B}$ drift, the second term is the magnetisation flux associated with Larmor rotation, the third term makes a small correction to the parallel guiding centre flux and is exactly compensated by the parallel component of the magnetisation flux. The last two terms describe the almost vertical drifts associated with the spatial variation of the magnetic field, namely the grad-$\boldsymbol{B}$ and curvature drifts. Being the curl of a vector, the magnetisation flux is divergence-free and thus drops out of particle transport equation. A similar expression can be written for the perpendicular momentum and energy fluxes. They also contain

* Corresponding author.
[1] E-mail: sardei@ipp.mpg.de.

0022-3115/99/$ – see front matter
PII: S0022-3115(98)00622-9

corresponding divergence-free magnetisation flux terms which drop out of the momentum and energy transport equations [8]. Thus the magnetisation fluxes do not lead to a redistribution of the plasma parameters nor to any asymmetry of particle and power deposition to the plates, as they do not carry fluxes to the material surfaces [10]. This is also supported by 2D particle kinetic simulations [11]. Therefore, the analysis can be restricted to the electric and vertical drifts. They mainly arise, respectively, from radial and poloidal temperature inhomogeneities and from the $1/R$ dependence of the main field.

2. Limiter configurations

2.1. Limiter SOL geometry

For W7-AS low ι (<0.4) configurations, smooth, resonant-free magnetic flux surfaces extend deeply into the SOL of two up/down symmetric rail limiters (Fig. 1(a)). The two limiters are positioned up/down symmetrically at two neighbouring 'elliptical' planes of symmetry and their aperture can be changed by shifting them vertically with respect to each other. For $\iota \approx 1/3$ and small limiter aperture, the SOL is governed by large flux bundles with connection lengths of 1, 2 and 3 toroidal transits (Fig. 1(b)). They originate, in the first two cases, from the mapping of the limiters onto each other, in the third case from the mapping of each limiter onto itself. The poloidal sequence of flux tubes with different connection lengths introduces a poloidal distribution of the plasma parameters in the SOL.

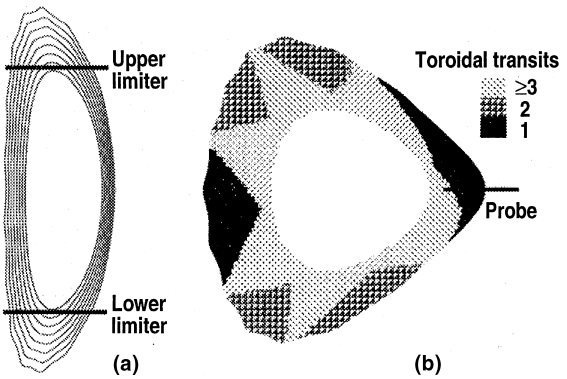

Fig. 1. (a) Two up/down symmetric rail limiters positioned at two neighbouring elliptical planes deeply cut the smooth flux surfaces of the $\iota \approx 1/3$ configuration. (b) Connection length distribution in the limiter SOL at a triangular plane. A Langmuir probe is placed horizontally at the outboard side of the configuration.

2.2. Up/down asymmetries

For low density, low recycling ECRH hydrogen plasma with small limiter aperture ($\langle n_e \rangle_{line} = 5 \times 10^{18}\ m^{-3}$, $Z_{lim} = 21.5$ cm), asymmetric and B-direction dependent power loads on the up/down limiters were typically found from calorimetric measurements. The observed ±20–30% up/down asymmetry is consistent with a parallel momentum imbalance driven by classical vertical particle drifts and can be estimated by a simple 1D parallel transport model. The ion vertical drift arising from the $1/R$ dependence of the toroidal field component is

$$n\boldsymbol{V}_d = \pm \frac{2p_i(1+M^2)}{eBR}\boldsymbol{z}^0, \tag{2}$$

where M is the Mach number, $p_i = p_{i\perp} \approx p_{i\parallel}$ and ± indicates the B-field direction.

For the given plasma parameters, the parallel temperature drop in the SOL is negligible. Poloidal diffusion of particles and momentum is also negligible, owing to the large ratio of poloidal to radial scale lengths for a limiter SOL. Radial loss of parallel momentum by viscosity and radial diffusion is also ignored, as it gives no up/down contributions. Assuming, for simplicity, a circular cross section, the parallel particle and momentum transport equations for the SOL region read [3]

$$\frac{\Theta}{r_a}\frac{\partial}{\partial\theta} nV_\parallel = S - \nabla_r \cdot n\boldsymbol{V}_d, \tag{3}$$

$$\frac{\Theta}{r_a}\frac{\partial}{\partial\theta} p(1+M^2) = -\nabla_r \cdot mn\boldsymbol{V}_\parallel \boldsymbol{V}_d \tag{4}$$

with θ the poloidal direction, Θ the pitch of B, r_a the radius of the last closed magnetic surface, S the particle source in the SOL due to radial diffusion from the main plasma and $p = 2p_e = 2p_i$. The radial gradients are represented by the respective gradient lengths, namely $1/\lambda_p$ for Eq. (3) and $1/\Delta_m$ for Eq. (4). Considering the case of a vertical drift directed upwards, substituting Eq. (2) into Eqs. (3) and (4) and integrating from the midplane to the lower limiter, we get for the relative momentum loss of ions, δ, as defined by

$$\frac{2p_{t,lower}}{p_0} = \frac{1}{1+\delta}, \tag{5}$$

the relation

$$\delta = \frac{1.5}{2}\frac{mC}{eB\iota\Delta_m}\left(\alpha + \frac{2T}{eB\iota\lambda_p C}\right), \tag{6}$$

where C is the sound speed and $\alpha = 0.82$ or 0.64 depending on whether the analysis refers to flux tubes mapping each limiter onto itself or mapping the two limiters onto each other. Assuming $\Delta_m = \lambda_p = 1$ cm, we get for the given plasma parameters $\delta = 0.29$ and 0.23 for the two flux tubes. This momentum loss for the ions

flowing to the lower limiter is due to a vertical drift directed radially inwards, i.e. into the confined region. No loss occurs for the ions flowing to the upper limiter, as they drift radially outwards, i.e. into the open field line region contacting the limiters. That is, the pressure at the upper limiter is $p_{t,upper} = p_0/2$. Neglecting parallel temperature gradients in the SOL, we then get for the power asymmetry $P_{load,upper}/P_{load,lower} = p_{t,upper}/p_{t,lower} = 1 + \delta$. This momentum imbalance is reversed if the B field is reversed.

2.3. Asymmetries of the radial density profiles

Additionally to the vertical drift discussed in the previous section, poloidal and radial $\boldsymbol{E} \times \boldsymbol{B}$ drifts arise in the limiter configuration shown in Fig. 1. The poloidal modulation of connection lengths shown in Fig. 1(b) implies a poloidal modulation of the radial decay lengths ($\lambda \propto L_c^{1/2}$) and hence of the radial plasma density and temperature profiles. Density profiles from low-density discharges, obtained from a Langmuir probe placed on the midplane at a triangular cross section (Fig. 1(b)), are shown in Fig. 2(a) for positive and negative B. In the absence of plasma, the probe intersects the boundary between flux tubes of longer and shorter connection lengths (Fig. 1(b)). A poloidal $\boldsymbol{E} \times \boldsymbol{B}$ drift arising from the radial temperature gradients tends to shift this boundary in positive or negative poloidal direction. Depending on the sign of B, flux tubes of longer or shorter L_c, i.e. of broader or steeper density profiles, are then "seen" by the probe (Fig. 2(a)). This effect has been reproduced by a 2D radial/poloidal model for particle and energy transport including the poloidal drift [3]:

$$\nabla_\perp(-D\nabla_\perp n + nV_{\boldsymbol{E}_r\times\boldsymbol{B}}) = S - \frac{nC}{L_c} \tag{7}$$

$$\nabla_\perp\{-(\chi_i + \chi_e)n\nabla_\perp T - 5TD\nabla_\perp n + 3nTV_{\boldsymbol{E}_r\times\boldsymbol{B}}\} = -\frac{\gamma nTC}{L_c}, \tag{8}$$

where L_c is the 2D distribution of connection lengths, $T = T_i = T_e$, $\chi = \chi_i + \chi_e$ ($\chi_i = \chi_e = 3D$, $D = 1$ m^2/s).

At the poloidal probe position, the calculations reproduce the change in the slope, i.e. in the decay length of the density profiles in the region from $r_{eff} = 14$ to 17 cm, as measured by the probe (Fig. 2(b)). Fig. 3 compares the density contours for positive and negative B calculated with this model in the relevant SOL region over the full poloidal angle. The plots clearly show the $\boldsymbol{E}_r \times \boldsymbol{B}$ driven poloidal phase shift of the radial density profiles corresponding to the flux tubes with $L_c = 1$, 2 and 3 toroidal transits. Similar results have been

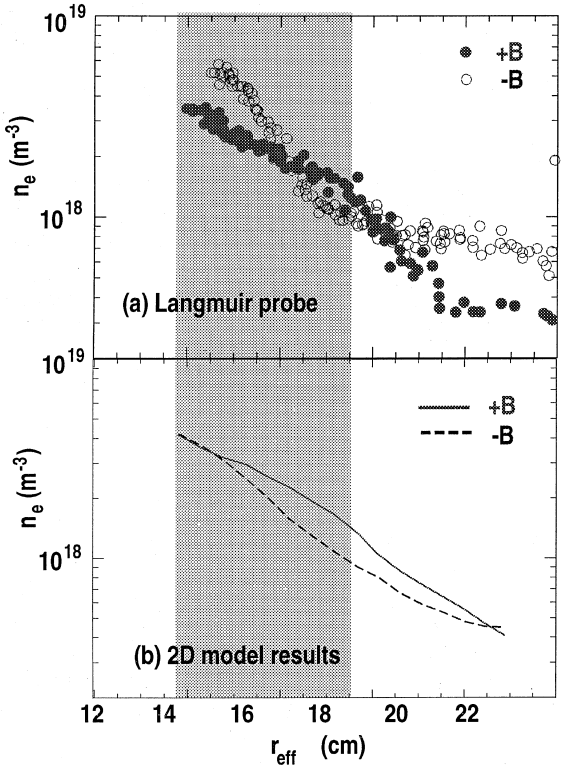

Fig. 2. (a) Field reversal effects (shoulder) on the density profiles from Langmuir probe data. (b) 2D simulation results. The shaded region is the radial transition zone between $L_c = 1$ and 3 toroidal transits.

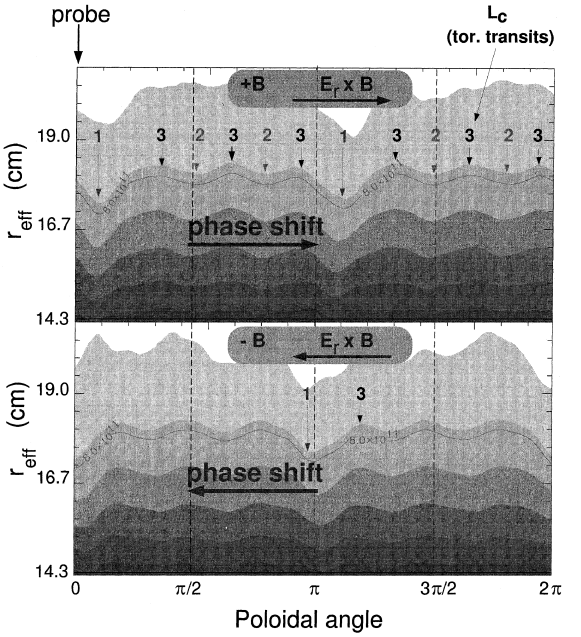

Fig. 3. Radial/poloidal density contours in the SOL for $\pm B$, showing poloidal modulations due to $L_c = 1$, 2, 3 toroidal transits.

obtained with more sophisticated 3D Monte Carlo transport simulations including the poloidal drift [1]. The profile variations in the outside SOL regions ($r_{\mathrm{eff}} > 17$), however, cannot be explained by a poloidal $\boldsymbol{E} \times \boldsymbol{B}$ drift. Here, radial $\boldsymbol{E} \times \boldsymbol{B}$ drifts resulting from the poloidal temperature modulation must be taken into account [12]. They lead to radially inward or outward drift flows depending on the magnetic field direction. These drifts modify the shape of the density profiles consistently with the probe data [3].

3. Island divertor configurations

3.1. Island SOL geometry

At $\iota \geqslant 0.5$, the boundary of W7-AS is governed by intrinsic magnetic islands of considerable size, which define the topology of the island divertor [13]. The $\iota = 5/9$ edge configuration, represented by a poloidal chain of nine islands, has been chosen for standard divertor operation, as it offers the best compromise between large plasma and large island size and has the appropriate internal rotational transform. The present target arrangement consists of 10 inboard target plates placed symmetrically on both sides of the triangular cross section. Each plate intersects two islands at a variable radial position which can be changed by ι and a vertical magnetic field. In the cases analysed here, the islands are cut through the O-point (Fig. 4).

3.2. Poloidal asymmetries

The discharges investigated are at very low density, $\langle n_e \rangle_{\mathrm{line}} < 10^{19}$ m^{-3}, and ECR heating power of about 200 kW. Fig. 4 compares the poloidal profiles of power deposition and particle outflux along the target plate from calorimetric and H_α measurements for positive and negative B. The profiles generally peak at the island (a), reflecting the larger connection length at this position. Here, the highest particle flux is found in the left SOL fan (contacting tile 1) of the island for positive B, in the right one (tile 2) for negative B. A similar behaviour is observed for the power deposition.

A corresponding B-dependent asymmetry is found for the density contours of a 2D Langmuir probe array located at the inboard side of the triangular cross section (Fig. 5(a)). The contour lines (Fig. 5(b)) reproduce correctly the poloidal structure of the vacuum island chain, but not its up/down symmetry (Fig. 5(a)). After reversing the field direction, the observed asymmetry is reversed as well. This effect can be explained by a poloidal $\boldsymbol{E} \times \boldsymbol{B}$ drift inside the islands as follows. For the low density conditions of the analysed discharges, ionisation mainly occurs in the main plasma. The recycled

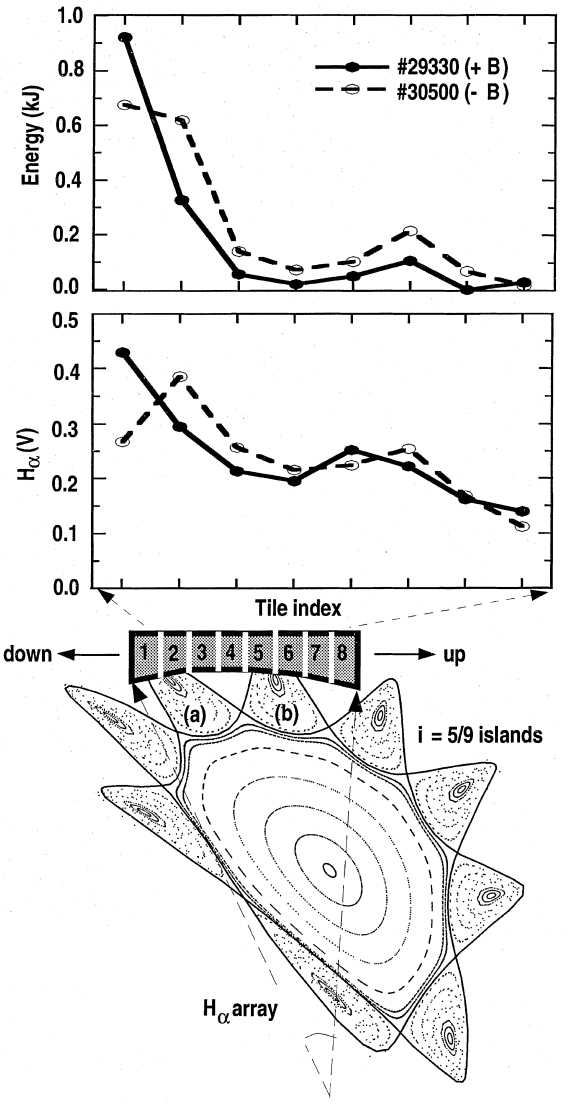

Fig. 4. (Top) Calorimetric and H_α profiles along the target plate for two discharges with $\pm B$. (Bottom) Poloidal cross-section of the $\iota = 5/9$ configuration at the toroidal position of a target plate.

particles diffuse outwards into the islands, where they experience a poloidal electric drift in addition to the parallel motion along the island fans. The drift originates from the radial electric field associated with the radial temperature drop from the separatrix to the O-point: $E = 3(T_{\mathrm{sep}} - T_{\mathrm{Op}})/e r_{\mathrm{isl}}$, r_{isl} being the average island radius at the separatrix. (The islands are intersected and electrically linked by the plates.) A particle accumulation results in the upper or lower island fans, depending on the field direction. From 3D transport simulations with the EMC3 code [14,15], the temperature difference between the island fan and the island core

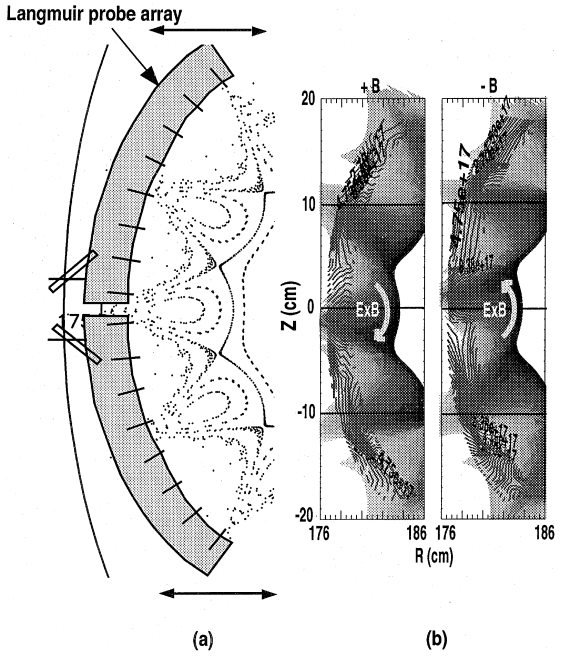

Fig. 5. (a) Moveable Langmuir probe array consisting of 16 probes placed on the inboard side of a triangular cross-section and shaped as to follow the magnetic edge structure. (b) Density contour lines from the probe array compared to calculated distributions (shaded areas) from the EMC3 code for $\pm B$.

is estimated to be about 20 eV, which leads to a poloidal drift of about 1.5 km/s.

In the following we show that this poloidal drift governs the particle transport in the islands. First of all, the almost vertical grad-B and curvature drifts have no relevance for asymmetries inside the islands, owing to the helical path of the islands around the torus. Furthermore, for a low density plasma the estimated total particle flow per toroidal unit length due to the poloidal drift, $(\Gamma_\theta)_{\rm tot} \approx 3\ T_{\rm e,down} n_{\rm e}/eB$ [4], dominates over the flow due to the radial drift, $(\Gamma_{\rm r})_{\rm tot} \approx (T_{\rm e,up} - T_{\rm e,down}) n_{\rm e}/eB$, because of the small poloidal variation of the temperature, $T_{\rm e,up} \approx 90$ eV and $T_{\rm e,down} \approx 60$ eV [2]. These are temperatures at the upstream and target positions, as estimated from EMC3 code simulations and Langmuir probe array data (downstream value). The impact of both drifts on the particle transport is stronger than in tokamak divertors for the same plasma parameters and major radius, due to the larger toroidal length of the X-line (poloidal periodicity of $N = 9$ for W7-AS compared to 1 for single-null tokamaks). As for the diffusive particle transport, the time scale for the particles to reach the targets by drift motion is $\tau_{\rm drift} = d_{\rm pol}/V_{E_r \times B} = 4.7 \times 10^{-5}$ s, which is much shorter than that by cross-field diffusion $\tau_{\rm diff} = (\Delta r)^2/(2D) = 8 \times 10^{-4}$ s, with $d_{\rm pol} = 7$ cm, $\Delta r = 4$ cm and $D = 1$ m^2/s. Finally, the poloidal drift velocity is also substantially larger than the poloidal component of the parallel velocity, owing to the very small pitch of the magnetic field in the island reference frame ($\sin\theta_{\rm i} \approx 0.001$). In fact, for a hydrogen sound speed consistent with $T \equiv T_{\rm i} = T_{\rm e} = 60$ eV, we get $C_{\rm t} \sin\theta_{\rm i} = 100$ m/s, which is more than an order of magnitude smaller than the estimated drift velocity. For the same reason, the drift energy flux dominates over the parallel convection energy flux. Therefore, the particle and energy transports are decoupled from the parallel momentum transport.

Based on these considerations, a simple 1D poloidal fluid transport model for particles ($\boldsymbol{E}_{\rm r} \times \boldsymbol{B}$ drift) and heat ($\boldsymbol{E}_{\rm r} \times \boldsymbol{B}$ drift and parallel heat conduction) has been defined [2]:

$$\frac{\mathrm{d}}{\mathrm{d}y}(nV_{E_{\rm r}\times \boldsymbol{B}}) = \left\{ S_{\rm p};\ 0;\ -\frac{nC_{\rm t}}{L_{\rm c}} - D\frac{n}{\Delta_{\rm r}\lambda_{\rm n}} \right\}, \tag{9}$$

$$\frac{\mathrm{d}}{\mathrm{d}y}\left(-\Theta^2 \kappa T^{\frac{5}{2}} \frac{\mathrm{d}T}{\mathrm{d}y} + 3nTV_{E_{\rm r}\times \boldsymbol{B}}\right) = \left\{ S_{\rm e};\ 0;\ -\frac{\gamma nTC_{\rm t}}{L_{\rm c}} - D\frac{5nT}{\Delta_{\rm r}\lambda_{\rm n}} - \chi\frac{nT}{\Delta_{\rm r}\lambda_T} \right\}, \tag{10}$$

where the first terms on the right-hand side of the equations represent the particle and energy diffusion sources from the main plasma into the SOL, the second terms the negligible losses in the region from the X-point to the target boundary, and the third terms the losses to the plates and to the private region.

The resulting enhancement (for positive B) and reduction (for negative B) factor of the density over the region covering the poloidal depth of the plate region is about a factor of two, which is in good agreement with the asymmetry of the probe array data. For the temperature, on the other hand, the calculated asymmetry is less than 30%, which is also consistent with the probe array measurements and reflects the predominance of the parallel conduction over the drift-convection for the considered low-density plasma. The asymmetry of the calculated power fluxes between the upper and lower island fans of the lower island is about a factor of 2.4, which is stronger than the measured asymmetry of the power load on the plate at the corresponding strike points (about 50%, see Fig. 4). This discrepancy is due both to the poor calorimetric resolution of the relatively large tiles and to the missing power load hitting the plates from the private region, which has not been accounted for by the 1D model. The described asymmetry of the poloidal densities and its inversion with reversed B direction is confirmed quantitatively by the poloidal phase shift of the density distribution obtained from a more rigorous 3D simulation with the EMC3 code after including the estimated poloidal drift velocity [2]. The shift (shaded picture in Fig. 5(b)) is in excellent agreement with that of the density from the Langmuir probe array data (contour lines in Fig. 5(b)).

A problem in particle control may arise from discontinuous target plates in the presence of a strong poloidal particle drift. In fact, if the particle transport is dominated by the poloidal drift and if the toroidal extension of the plates is small, which is the case for the low-density discharges presented here, a significant fraction of the particle flux can drift poloidally outwards in the toroidal regions between the plates. This may be crucial if these drifting particles diffuse into open field lines (like those in the private region or in open island structures). A careful optimisation of the plate design would be necessary if the problem persists for divertor-relevant high density conditions. On the other hand, higher densities imply lower downstream temperatures, which should reduce, according to simple estimates, the average radial electric field and thus the poloidal $\boldsymbol{E} \times \boldsymbol{B}$ drift in favour of the radial $\boldsymbol{E} \times \boldsymbol{B}$ drift. However, for large parallel temperature gradients and high recycling inside the islands, the electric field becomes fully 3D in the presence of discontinuous target plates. This makes its determination a non-trivial task both experimentally and numerically. Langmuir probe array data for high density conditions do not indicate sharply outlined poloidal asymmetries of the density contours nor simple reversal of the asymmetries with reversed field direction. Therefore, a definitive assessment of the classical drift effects on plasma transport for divertor-relevant conditions is not possible on the basis of the data available so far.

4. Conclusions

Classical grad-B and $\boldsymbol{E} \times \boldsymbol{B}$ drifts have been shown to significantly perturb the symmetry of up/down limiter power loads and plasma density distributions in limiter and island divertor configurations for low density, high temperature ECRH discharges in W7-AS. For these plasma conditions, the poloidal $\boldsymbol{E} \times \boldsymbol{B}$ drift arising from radial temperature gradients inside the islands dominates not only over the radial $\boldsymbol{E} \times \boldsymbol{B}$ drift, but also over the poloidal component of the parallel motion, which no longer determines the particle transport. A parallel particle mapping onto the target plates becomes questionable in this case. The effects of the vertical and electric drifts on the plasma transport in both limiter and island configurations can be described with sufficient accuracy by relatively simple 1D and 2D models, and are confirmed by more rigorous 3D code simulations. For divertor-relevant high density conditions, lower target temperatures should reduce the magnitude of the poloidal electric drift, but parallel temperature gradients will lead to inhomogeneous poloidal and toroidal distribution of the radial electric field. A 3D resolving diagnostic of the plasma parameters will be needed for divertor-relevant plasma conditions to reliably estimate the impact of the electric drifts on the power exhaust and particle control in W7-AS and W7-X. A self-consistent 3D treatment of the drifts will also be needed, which is beyond the present capability of the EMC3 code.

References

[1] Y. Feng et al., in: Proceedings of the 22nd EPS Bournemouth, UK, vol. 19C, 1995, p. 325.
[2] Y. Feng et al., Plasma Phys. Control Fusion 40 (1998) 371.
[3] Y. Feng et al., Contr. Plasma Phys. 38 (1998) 195.
[4] A.V. Chankin et al., Plasma Phys. Control Fusion 36 (1994) 1853.
[5] A.V. Chankin, J. Nucl. Mater. 241–243 (1997) 199.
[6] T.D. Rognlien et al., J. Nucl. Mater. 196–198 (1992) 347.
[7] M. Baelmans et al., J. Nucl. Mater. 220–222 (1995) 982.
[8] G.J. Radford et al., Contr. Plasma Phys. 36 (1996) 187.
[9] S.I. Braginskii, in: M.A. Leontovich (Ed.), Reviews of Plasma Physics, vol. 1, Consultants Bureau, New York, 1965, p. 205.
[10] A.V. Chankin, P.C. Stangeby, Plasma Phys. Control Fusion 36 (1994) 1485.
[11] A. Bergmann, R. Chodura, Contr. Plasma Phys. 36 (1996) 220.
[12] F. Sardei et al., J. Nucl. Mater. 220–222 (1995) 736.
[13] F. Sardei et al., J. Nucl. Mater. 241–243 (1997) 135.
[14] Y. Feng et al., J. Nucl. Mater. 241–243 (1997) 930.
[15] Y. Feng et al., these Proceedings.